Nano Energy 60 (2019) 312–323

Contents lists available at ScienceDirect

Nano Energy

journal homepage: www.elsevier.com/locate/nanoen

Full paper

Nanoflake-constructed porous $Na_3V_2(PO_4)_3$/C hierarchical microspheres as a bicontinuous cathode for sodium-ion batteries applications

Xinxin Cao[a], Anqiang Pan[a,*], Bo Yin[a], Guozhao Fang[a], Yaping Wang[a], Xiangzhong Kong[a], Ting Zhu[a], Jiang Zhou[a,**], Guozhong Cao[b], Shuquan Liang[a,***]

[a] School of Material Science and Engineering, Central South University, Changsha, Hunan, 410083, China
[b] Department of Materials Science & Engineering, University of Washington, Seattle, WA, 98195, United States

ARTICLE INFO

Keywords:
$Na_3V_2(PO_4)_3$
Microsphere
Hierarchical structure
N-doped carbon
Sodium-ion battery

ABSTRACT

Sodium-ion batteries (SIBs) have attracted considerable attention for large-scale energy storage systems as a promising alternative to lithium-ion batteries (LIBs) due to the huge availability and low-cost. Yet the development of SIBs has been hindered by the low reversibility, sluggish ion diffusion, as well as large volume variations. Herein, we report an efficient hydrothermal method for fabricating hierarchical porous $Na_3V_2(PO_4)_3$/C (NVP/C) microspheres assembled from interconnected nanoflakes. The NVP nanocrystals are uniformly wrapped by N-doped carbon layer. As a half-cell cathode, the NVP/C porous microspheres exhibit superior rate capability (99.3 mA h g^{-1} at 100 C) and excellent cyclic stability (79.1% capacity retention over 10,000 cycles at 20 C). A full-cell configuration coupled with NVP/C cathode and SnS/C fibers anode exhibits an estimated practical energy density of 223 W h kg^{-1}. The superior performance can be ascribed to the hierarchical porous micro/nano structure along with N-doped carbon encapsulation, which provide bicontinuous electron/ion pathways, large electrode-electrolyte contact area, as well as robust structural integrity. This work provides a promising approach for boosting the electrochemical performance of battery materials via the integration of hierarchical structure and heteroatoms doped carbon coating.

1. Introduction

Large-scale energy storage systems (ESSs) for sustainable and renewable energy resources, such as solar energy and wind power, have attracted significant attention with the increasing environmental concerns and energy shortages [1,2]. Among the various candidates for ESSs, rechargeable LIBs have received considerable attention and have been applied successfully in large-scale grid with prominent advantages of high energy density, high energy conversion efficiency, and simple maintenance, but typically face challenges of insufficient service life, and the potential limitation of lithium terrestrial reserves [3–6]. SIBs have attracted increasing research attention as an alternative power device for large-scale ESSs due to its abundant resources in storage [7–9]. Furthermore, owing to the similar ion insertion chemistry to LIBs, the already-established materials design theories and processes for LIBs can be used to stimulate the rapid development of SIBs. Nevertheless, some intrinsic drawbacks should be addressed before their actual applications in large-scale ESSs [10]. For instance, the ionic radius of Na^+ (coordination number 6: 1.02 Å) is about 34% larger than Li^+ (coordination number 6: 0.76 Å), which results in an inferior reversibility and sluggish ion diffusion [11]. Besides, the larger Na^+ leads to larger volume expansion/contraction and severer structural distortion of the host materials [12]. Consequently, electrode materials with sufficiently large interstitial space and open crystallographic structure are highly recommended for fast sodium ion storage.

To date, a large variety of materials, such as transition metal oxides [13–15], polyanionic compounds [16–19], ferrocyanide materials [20,21], and organic compounds [22–24], have been extensively investigated as sodium hosts. Among them, sodium super ionic conductor (NASICON) structured $Na_3V_2(PO_4)_3$/C is considered to be one of the most promising cathode candidates in terms of its excellent structural stability, high redox potential (about 3.4 V vs. Na^+/Na), good thermal stability (up to 450 °C), and large theoretical energy density (about 394 W h kg^{-1}) [25,26]. Moreover, the NASICON structure with an open three-dimensional (3D) framework has large interstitial channels for rapid Na^+ migration. However, similar to other isomorphism

* Corresponding author.
** Corresponding author.
*** Corresponding author.
E-mail addresses: pananqiang@csu.edu.cn (A. Pan), zhou_jiang@csu.edu.cn (J. Zhou), lsq@csu.edu.cn (S. Liang).

https://doi.org/10.1016/j.nanoen.2019.03.066
Received 9 February 2019; Received in revised form 19 March 2019; Accepted 19 March 2019
Available online 22 March 2019

compounds (i.e. $Li_3V_2(PO_4)_3$, $NaTi_2(PO_4)_3$, and $K_3V_2(PO_4)_3$) [27–29], NVP suffers from intrinsically inferior electronic conductivity (about 10^{-9} S cm^{-1}) [16,17], which greatly limits its further practical application, especially in large-scale ESSs when durability is a prerequisite.

Construction of NVP/carbon composites has been demonstrated as an effective way to improve the electronic conductivity and electrochemical performance. Fang et al. reported a hierarchical carbon framework wrapped NVP with ultra-high rate capability and ultra-long cycling stability of 20,000 cycles at 30 C in SIBs [30]. Rui et al. designed a convenient freeze-drying-assisted strategy to construct a double-carbon decorated NVP with excellent rate capability of 86 mA h g^{-1} at 100 C [31]. Although this technique has been widely used for improving the conductivity of electrode materials, homogeneously distributed surface coatings are very difficult to achieve and too thick coating layer may restrict the easy penetration of ions. Coating by a medium layer that conducts electrons but does not prevent ionic access (e.g., heteroatoms doped carbon materials) is the ideal choice [32,33].

In addition, for a highly efficient sodium storage process, it involves not only electronic conduction but also ionic transport in the electrode materials. Nanostructured NVP are commonly prepared to improve the sodium ion transport kinetics in the host materials due to the reduced Na^+ diffusion distance. Ren et al. reported a self-sacrificed route to fabricate 3D NVP nanofiber network with the capacity retention of approximately 95.9% after 1000 cycles at 10 C for SIBs [34]. Zhou et al. reported template-assisted preparation of nanostructured NVP 3D foams, which exhibit almost no capacity loss over 1000 cycles at a rate of 100 C [35]. However, there are also some disadvantages associated with these nanostructured active materials compared to micro-sized particles, such as lower tap densities, easier irregular aggregation, and more severe adverse surface side reactions, which lead to the low volumetric energy density and poor cyclic stability [36,37]. In this respect, the best way to achieve both high rate capability and high tap density is to develop a micro/nano hierarchical structure, that is, micrometer-sized particles composed of self-assembled nanosized particles with sufficient pores or channels. It is still highly desirable to design an ideal-structured NVP/C composite with substantially improved electronic and ionic transport kinetics as well as high tap density for large-scale ESSs applications.

Herein, we first present a facile and controllable strategy for the synthesis of nanoflake-constructed porous NVP hierarchical microspheres (NVP/C-MSs) accompanied with a N-doped carbon coating. Based on time-dependent experiments, a surfactant-guided self-assembly and continuous dissolution & recrystallization morphological evolution mechanism is proposed. As illustrated in Fig. S1a (Supporting Information), such a unique N-doped carbon modified porous structure provides favorable kinetics for both electron and Na^+. Therefore, by combining bicontinuous electron/ion pathways, large active contact area, and excellent structure integrity, nearly theoretical capacity and excellent rate capability as well as stable cycling performance are simultaneously achieved for NVP/C-MSs. In addition, an advanced sodium-ion full-cell based on the NVP/C-MSs cathode and SnS/C fibers anode delivers a high specific capacity and good cycling stability, indicative of its potential applications as a promising cathode candidate directed to large-scale ESSs markets.

2. Experimental section

2.1. Materials preparation

All reagents and solvents including vanadium(V) oxide (V_2O_5, ≥99.0%), sodium oleate ($C_{18}H_{33}NaO_2$, ≥98.0%), ammonium dihydrogen phosphate ($NH_4H_2PO_4$, ≥99.0%), urea (CH_4N_2O, ≥99.0%), hydrogen peroxide (H_2O_2, ≥30.0%) were of analytical grade and were used without further purification. In a typical procedure, initially, 0.1102 g vanadium(V) oxide was dispersed in 18 mL deionized water, followed by adding 2 mL hydrogen peroxide dropwise under vigorous stirring for 1 h at room temperature. The obtained bright yellow solution was denoted as A. Secondly, 0.2091g ammonium dihydrogen phosphate and 0.2796 g urea were dissolved in deionized water (20 mL) in a three-necked round-bottom flask fitted with a reflux condenser and stirring bar under stirring for 10 min, 0.5872 g sodium oleate was then added and dispersed with continuous stirring at room temperature for 1 h. The as-obtained homogenous milk solution was denoted as B. Afterwards, solution A was added dropwise into solution B under vigorous stirring and further refluxed at 80 °C for 10 h using an oil bath. During this procedure, the color of the solution turned from saffron yellow to invisible green gradually. Subsequently, the as-prepared mixture solution was transferred into a Teflon-lined stainless-steel autoclave with a capacity of 50 mL. The autoclave was sealed and placed in an oven at 200 °C for 48 h, followed by cooling to room temperature naturally for several hours. Under these hydrothermal conditions, the components self-assembled into a cylindrical NVP/C hydrogel. This hydrogel was rinsed with deionized water for 3 times, followed by a freeze-drying process, forming porous NVP/C aerogel. Finally, the obtained aerogels were annealed at 800 °C for 8 h at the ramping rate of 2 °C min^{-1} under a pure argon flow to yield the black NVP/C-MSs product.

For comparison, NVP/C samples were prepared under the same hydrothermal conditions and calcination process as applied in the synthesis of NVP/C-MSs except concentrations of precursor solution. Additionally, in order to investigate the effects of hydrothermal time on the morphologies and microstructures of the NVP/C samples, other samples were also prepared under different hydrothermal time. The detailed experimental parameters are displayed in Table 1.

2.2. Materials characterization

The morphologies, microstructures, and crystallinity of the obtained samples were observed via field emission scanning electron microscopy (FESEM, FEI Nova NanoSEM 230, 10 kV) and transmission electron microscopy (TEM, FEI Tecnai G2 F20, 200 kV) equipped with an X-ray energy-dispersive spectrometer (EDS). The crystal structures of the samples were identified by using X-ray diffractometer (Rigaku D/Max-2500 with Cu-Kα radiation, λ = 1.5418 Å). A step scan was used with a step size of 0.02° and a count time of 2 s. The carbon contents of the samples were determined by a thermal-gravimetric analyzer (Netzsch STA 449 C) and the property of coated carbon layer was analyzed by Raman microspectrometer (LabRAM HR800 with a laser wavelength of 532 nm). The electronic states of elements in the surface were also

Table 1
The denoted name of different kinds of NVP samples.

Hydrothermal time	Concentration of the target product in each reaction kettle				
	0.005 M	0.01 M	0.015 M	0.02 M	0.025 M
6 h			NVP/C-15-6		NVP/C-25-6
12 h			NVP/C-15-12		NVP/C-25-12
24 h			NVP/C-15-24		NVP/C-25-24
36 h			NVP/C-15-36		NVP/C-25-36
48 h	NVP/C-5-48	NVP/C-10-48	NVP/C-MSs (NVP/C-15-48)	NVP/C-20-48	NVP/C-25-48

probed by X-ray photoelectron spectrometer (VG Escalab-250xi). Carbon and nitrogen contents in the NVP/C products were also determined using LECO analyses (TCH-600 N/H/O analyzer and CS-600 C/S analyzer). N_2 adsorption/desorption isotherms of the samples were obtained from a surface area and porosity analyzer (ASAP 2460, Micromeritics) at 77K. The specific surface areas were analyzed using the Brunauer-Emmett-Teller (BET) theory. The pore size distributions were calculated using the Barrett-Joyner-Halenda (BJH) method. Fourier transform-infrared (FT-IR) spectra were also obtained on a FT-IR spectrometer (Nicolet 6700, Thermo Electron Scientific Instruments) to collect the information from the vibration or stretch of the functional groups in the samples.

2.3. Electrode fabrication and electrochemical measurement

The electrochemical measurements were carried out by assembly of standard CR2016-type coin cells in an argon-filled glove box (Mbraun, Germany). Working electrodes were prepared by coating a slurry mixed of active materials (75 wt%), conductive carbon (Super P) (15 wt%), and polyvinylidene fluoride (PVDF) (10 wt%) in N-methyl-2-pyrrolidone (NMP) onto an aluminum foil and dried in a vacuum oven at 100 °C overnight. The typical thickness of the electrode is ~30 μm with a mass loading of about 1.3 ± 0.2 mg cm^{-2}. For SIBs half-cell fabrication, metallic sodium foil as the both reference and counter electrodes, 1 M $NaClO_4$ in propylene carbonate (PC) with 5% fluoroethylene carbonate (FEC) additive was used as the electrolyte, and a Whatman glass fiber membrane (GF/D) was used as the separator. For the full-cell configuration, the cathode-active material was NVP/C-MSs. The SnS/C fibers served as the anode. A presodiation procedure was carried out for SnS/C anodes by applying two-times of discharge-charge cycles in half cells to compensate the initial irreversible capacity. The cell balance was achieved by setting the electrode mass ratio of cathode/anode to ~5:1. Both the charge and discharge current density and specific capacity were calculated based on the mass of cathode-active material. Galvanostatic charge/discharge measurements were carried out at different current densities using a multichannel battery testing system (LAND CT2001A, China). The cyclic voltammetry (CV) tests were carried out on an electrochemical workstation (CHI660E, China) at different scanning rates. Electrochemical impedance spectra (EIS) was performed on a Zahner electrochemical workstation (IM6ex, Germany). The frequency range was scanned from 100 kHz to 10 mHz, and the magnitude of the alternative signal was 5 mV.

3. Results and discussion

A schematic depiction of the synthesis process is displayed in Fig. S1b (Supporting Information). Sodium oleate with a carboxyl group and nonpolar tail is used as both sodium source and structure-directing agent for the synthesis of NVP/C microspheres. Hydrothermal treatment of the mixture solution at 200 °C for 48 h leads to the formation of amorphous microsphere precursor (Fig. S2, Supporting Information). Then the NVP aerogel precursor is obtained after freeze-drying (Fig. S3, Supporting Information). After annealing in a pure argon flow, the well-crystallized NVP/C-MSs product is obtained. The detailed morphological and crystallographic properties of the NVP/C-MSs composite are elucidated through FESEM and TEM. As shown in Fig. 1a and b, the NVP/C-MSs well inherits the hierarchical microsphere morphology of the precursors (Fig. S2, Supporting Information) and the microspheres have an average diameter of ~10 μm. No perceptible structural collapse or breakage is observed even after high-temperature annealing at 800 °C. The enlarged FESEM image (Fig. 1c) further reveals the detailed features of the microspheres, which are composed of nanoflakes with an approximately thickness of 20–30 nm. In addition, the adjacent nanoflakes are loosely interconnected with apparent open spaces between them. The TEM image (Fig. 1d) clearly demonstrates the completely solid and dense interior structure of the NVP/C microspheres, which is beneficial to increase the tap density of the electrodes. The continuous nanoflakes are radially oriented, and served as the building blocks to construct the hierarchical structure (Fig. 1e). The high-resolution TEM (HRTEM) image (Fig. 1f) clearly shows the lattice fringes with the space of 6.2 Å, corresponding to the (012) crystal plane of rhombohedral NVP. Notably, a uniform thin carbon layer of around 3 nm is well decorated on the surface of NVP crystal. The pure carbon skeleton can be obtained via the corrosion of NVP/C-MSs composite in the hydrofluoric acid to further confirm the 3D hierarchical carbon network. The energy dispersive X-ray (EDX) spectrum (the inset of Fig. 1g) demonstrates that NVP crystals are totally removed and only a carbon matrix is well preserved. After leaching, the morphology of hierarchical microsphere is well-maintained (Fig. 1g). Moreover, numerous void spaces are distributed in the carbon matrix (Fig. 1h). From the HRTEM image (Fig. 1i), interlayer spacing of 3.9 Å is clearly observed, indicating that the 3D carbon matrix is suitable to insert Na^+. Furthermore, the elemental mapping images confirm the existence and uniform distribution of Na, V, P, C, and N in the NVP/C-MSs composite as well (Fig. 1j).

The X-ray diffraction (XRD) pattern with Rietveld refinement (using GSAS-EXPGUI software package) of the as prepared NVP/C-MSs composite is shown in Fig. 2a. All the diffraction peaks of the pattern can be well-indexed to a pure rhombohedral $Na_3V_2(PO_4)_3$ phase (space group: $R\bar{3}c$) with lattice parameters a = 8.7368 Å, b = 8.7368 Å, c = 21.834 Å, and γ = 120.00° (ICSD#98-024-8140), indicating the high purity of the as-synthesized product. The lattice parameters and other structural information, including the atomic positions of the NASICON structure, are listed in Tables S1 and S2 (Supporting Information). Raman scattering spectrum was recorded to confirm the existence of carbon in the composite (Fig. 2b). Two characteristic bands of carbonaceous materials can be obviously observed, locating around at 1326 cm^{-1} (D-band, disorder-induced phonon mode) and 1588 cm^{-1} (G-band, E_{2g} vibrations of graphite). The I_D/I_G value of NVP/C-MSs is 1.18, which indicates the existence and partial graphitization of carbon in the composite [38]. The PO_4^{3-} signals are not distinguished in Raman spectrum because the signals are masked by the tightly wrapped carbon layer. Determined by the thermogravimetric analysis (TGA), the content of carbon in the NVP/C-MSs composite is about 9.72 wt% (Fig. S4, Supporting Information). Additionally, FT-IR spectrum is recorded as shown in Fig. S5 (Supporting Information). The characteristic bands for P-O stretching and V^{3+}-O^{2-} stretching are in accordance with previous literature [35,39]. As-prepared composite showed characteristic -COOH/-CN, -OH bands centered at wavenumbers of 1630 cm^{-1} and 3446 cm^{-1}, respectively, indicating the existence of the functional groups in carbon skeleton [28,40].

X-ray photoelectron spectroscopy (XPS) measurements were also conducted to unfold the surface chemical-bonding state of the NVP/C-MSs composite. The survey scan XPS spectrum (Fig. 2c) shows the presence of Na 1s, V 2p, P 2s, P 2p, O 1s, C 1s, and N 1s, with no evidence of impurities. The high resolution XPS spectrum of the V 2p doublet with two peaks located at 517.3 eV for V 2p3/2 and 524.3 eV for V 2p1/2, corresponding to the V^{3+} chemical states (Fig. S6, Supporting Information) [41,42]. The high resolution XPS C 1s spectrum (Fig. 2d) can be resolved into four components centered at 284.8, 285.8, 286.9, and 289.6 eV. The main peak located at 284.8 eV corresponds to the graphite-like sp^2 C [43]. The small peaks at 285.8 and 286.9 eV can be ascribed to the different bonding states of C-N bonds, corresponding to the N-sp^2 C and N-sp^3 C bonds, respectively, which would originate from the substitutional doping of N atoms [44]. The peak at 289.6 eV is identified as originating from CO type bonds. The high resolution XPS N 1s spectrum in Fig. 2e is deconvoluted into three peaks at 398.4, 400.3, and 401.5 eV, which can be assigned to pyridinic-N, pyrrolic-N, and graphitic-N, respectively [45]. In addition, elemental analysis shows the mass content of N is about 2.37% (Table S3, Supporting Information). Nitrogen isothermal adsorption/desorption measurement was also carried out to further characterize the porous structure of the NVP/C-MSs composite (Fig. 2f). The isotherm

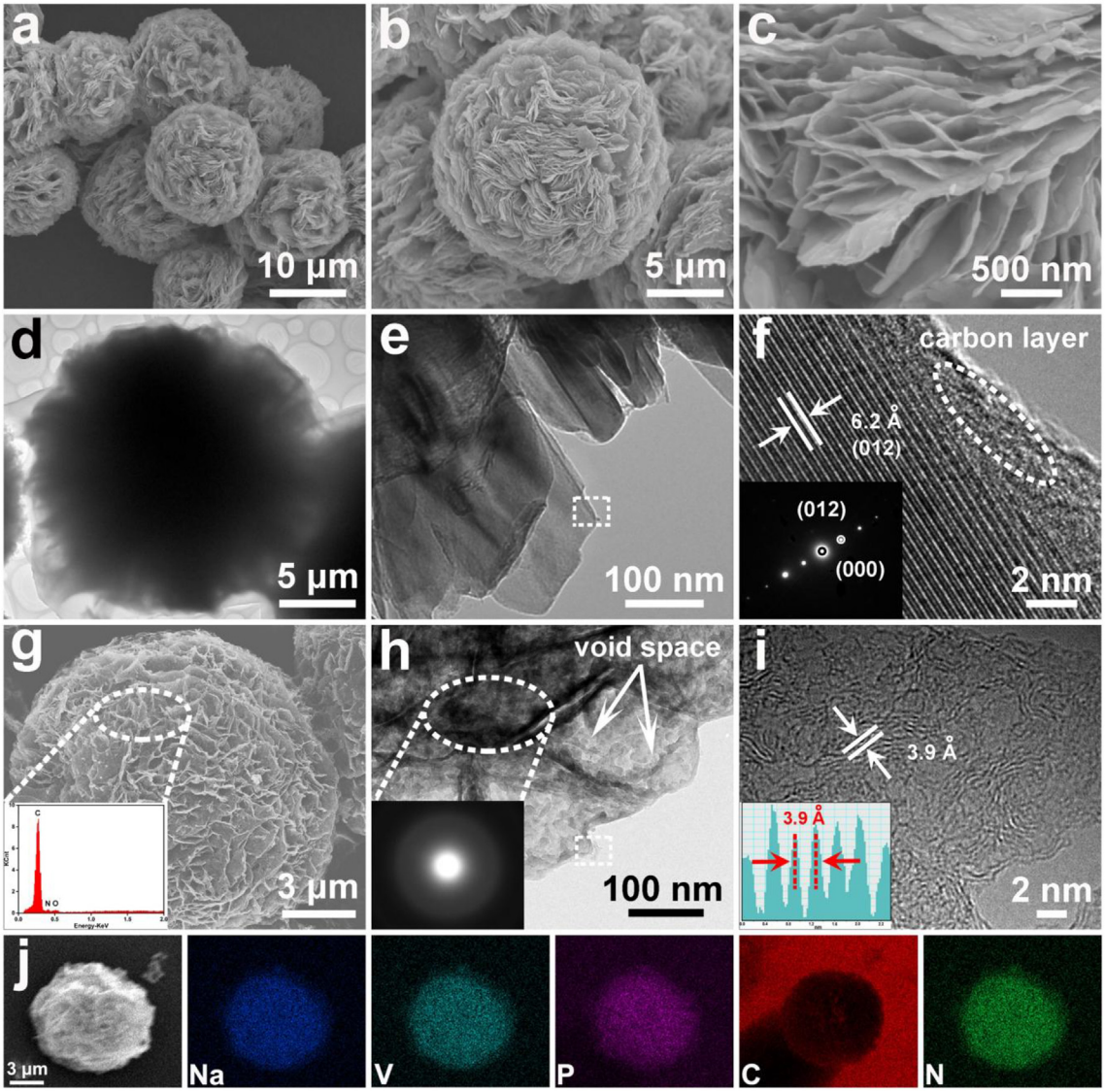

Fig. 1. The morphological and microstructural characterizations of the as-prepared NVP/C-MSs and the residual carbon scaffold after the corrosion of NVP nanocrystals. (a–c) FESEM images at different magnifications. (d, e) TEM images at low and high magnifications. (f) HRTEM image and the corresponding SAED pattern (the inset of panel (f)). Clear lattices with spacing of 6.2 Å is assigned to the (012) plane of NVP. (g) FESEM image, (h) TEM image, and (i) HRTEM image of the residual carbon scaffold. The insets of (g) and (h) are the EDX spectrum and SAED pattern of the selected regions, respectively. The inset of (i) shows an interplanar spacing of 3.9 Å. (j) EDX mapping area and corresponding elemental distributions of Na, V, P, C and N of a single NVP microsphere.

can be described as type II with type-H3 hysteresis loop, which can be linked to slit-shaped pores in the sample. The BET surface area of NVP/C-MSs is measured to be 44.78 $m^2 g^{-1}$. The BJH pore-size distribution curve (the inset of Fig. 2f) exhibits a broad pore size ranging from 3 to 40 nm. The pores are mainly contributed from the interstices among the assembled nanoflakes.

Time-dependent experiments were carried out to elucidate the morphological evolution process of hierarchical NVP/C products. FESEM and TEM images of the as-synthesized products obtained at different reaction durations are presented in Fig. 3. With a hydrothermal reaction time of 6 h, as shown in Fig. 3a1-a4, the fast nucleation and crystal growth processes lead to the formation of the irregular flower-like structure, which contains several loosely packed nanoflakes with a diameter of 1.5 μm and a thickness of 20–40 nm. When the time increased to 12 h, a mass of initial nanoflakes begin growing and aggregating together to form a spheroidal architecture (Fig. 3b1-b4). As the hydrothermal reaction time increased to 24 h (Fig. 3c1-c4), nanoflakes-constructed microspheres are formed to minimize the overall surface free energy. The microspheres have a diameter of 4–5 μm and the nanoflake building blocks show a thickness of 30–40 nm. Upon increasing the hydrothermal reaction time to 36 h (Fig. 3d1-d4), the initial microspheres undergo growth and final formation, accompanied by the recrystallization process to form a much denser internal. Finally, hierarchical microspheres are entirely evolved as the hydrothermal reaction further proceeded to 48 h (Fig. 3e1-e4). The as-prepared microspheres are highly uniform with a diameter of about 10 μm, which are constructed by a large amount of radially standing nanoflakes with a small thickness of about 25 nm. The arrangement of assembled nanoflakes is highly compact which can make full use of the limited space. In order to further verify the morphological evolution mechanism, the SEM images of the products obtained from a larger concentration are presented in Fig. S7 (Supporting Information). The result shows a similar morphological evolution process as a function of hydrothermal reaction time.

The 3D hierarchical architectures of the NVP/C products can also be tuned by adjusting the concentrations of the precursor solutions. As shown in Fig. 4, the concentrations of the precursors in each reaction kettle have little effect on the size of the microspheric products, and the

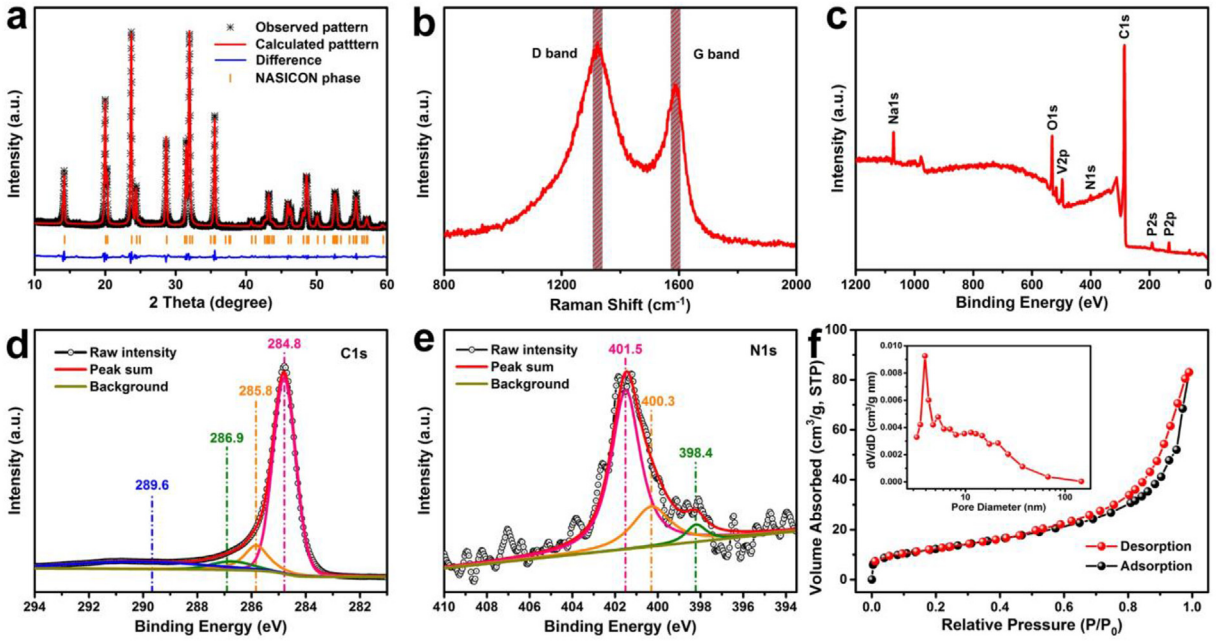

Fig. 2. The chemical and physical characterizations of the as-prepared NVP/C-MSs. (a) X-ray diffraction pattern with Rietveld refinement. (b) Raman scattering spectrum show clear D and G band with a relatively small D-/G-band peak intensity ratios, indicating the coated carbon is partially graphitized. (c) Survey scan XPS spectrum. (d, e) High-resolution XPS spectra of C 1s and N 1s. In (d), the fitted peaks correspond to graphite-like sp^2 C (284.8 eV), N-sp^2 C (285.8 eV), N-sp^3 C (286.9 eV) and CO type bond (289.6 eV). In (e), the fitted peaks correspond to pyridinic N (398.4 eV), pyrrolic N (400.3 eV), and graphitic N (401.5 eV). (f) Nitrogen adsorption-desorption isotherms. The inset of (f) shows the average pore size (3.5 nm) and pore size distribution derived from the adsorption branch by the BJH method.

mean diameter of the microspheres is about 10 μm. However, different reaction conditions have a great influence on the hierarchical structure, specifically on the nanoscale building blocks. Typically, the solid microspheres are constructed from entangled and randomly curved NVP/C ultrathin nanosheets, when the concentration of the target product is 0.005 M (Fig. 4a1-a5). When a concentration of 0.01 M is used, 3D hierarchical microspheres with large nanoflakes are formed and the thickness of the nanoflakes can be more than 20 nm (Fig. 4b1-b5). When a higher concentration (0.02 M) is used, the resulting microspheric product is formed by stacking ultra-thick nanoplates with almost no voids between them (Fig. 4d1-d5). Further increasing the concentration of the target product to 0.25 M leads to formation of nanoparticle assembled NVP/C microspheres (Fig. 4e1-e5).

It has been reported that nanostructured materials can be self-assembled into microstructures through an oriented aggregation mechanism [46–49]. On the basis of the above SEM and TEM observations, a possible formation process is schematically depicted in Fig. 5 and Fig. S1b (Supporting Information). Herein, sodium oleate with high-polarity carboxyl group and a nonpolar tail is used as both sodium source and structure-directing agent for the NVP/C microspheres synthesis. Simultaneously, the long alkyl chain in sodium oleate acts as carbon source to form the carbon skeleton along with the crystallization of NVP. First, a diluted sol of $V_2O_5{\cdot}nH_2O$ was prepared by dissolving V_2O_5 and hydrogen peroxide in deionized water [50]. Second, the $V_2O_5{\cdot}nH_2O$ sols was added into a mixed solution of sodium oleate, $NH_4H_2PO_4$, and urea to form sodium-vanadium-phosphate hydrophilic colloids with cationic surface. During stirring process under oil bath, the added anionic surfactant sodium oleate captured the cationic sodium-vanadium-phosphate colloids, accompanied by the rearrangement of charge density and formation of composite micelles [51,52]. During hydrothermal process, numerous precursor nuclei formed quickly and then grew into flaky nanocrystals directed by the surfactant. Afterwards, the aggregated nuclei serve as nucleation centers to allow the subsequent adsorption of newly formed nuclei and the growth of primary crystals [53]. Following, these freshly formed nanocrystals were not thermodynamically stable, and thus they would gradually self-assemble and form micro-structured spheres to minimize the interfacial energy [54,55]. As reaction time prolongs, the primary crystals underwent a process of continuous dissolution and recrystallization to make best use of the limited space. Finally, the as-prepared microsphere precursor was annealed to crystallize the NVP with the release and *in situ* carbonization of organic compounds. Interestingly, as the concentrations of the precursors increased, the size of the building blocks increased gradually and the void between the blocks decreased simultaneously. Using sodium acetate instead of sodium oleate as sodium source, only irregular NVP nano-particles were obtained (Fig. S8, Supporting Information).

The concentration of the precursor solution is a key factor that determines the micro/nanostructure of the NVP/C materials. For comparison, the products obtained at different concentrations were also studied and analyzed. XRD patterns of NVP/C products (Fig. S9, Supporting Information) also manifest high purity and crystallinity, similar to that of NVP/C-MSs. Table S1 (Supporting Information) shows the refined cell parameters of NVP with NASICON structure in the prepared samples, which correspond well with the previously reports [26,56,57]. The pore size distributions and specific surface areas of the NVP/C products are investigated by nitrogen sorption analysis (Fig. 2f; Fig. S10, Supporting Information). Among the five samples (Table S4, Supporting Information), NVP/C-MSs possesses the highest BET surface area of 44.78 $m^2\,g^{-1}$, which is slightly larger than that of NVP/C-5-48 (33.28 $m^2\,g^{-1}$) and NVP/C-10-48 (27.81 $m^2\,g^{-1}$), while the BET surface areas of NVP/C-20-48 and NVP/C-25-48 are only 18.32 $m^2\,g^{-1}$ and 10.11 $m^2\,g^{-1}$, respectively. In addition, owing to the space-efficient packing inside secondary particles, the NVP/C-MSs shows the smallest volume occupied among the five samples obtained from different hydrothermal reaction time with the same mass (Fig. S11a, Supporting Information). Fig. S11b (Supporting Information) shows the volume occupied comparison of the NVP/C products with different building blocks and compactness. The low volumetric occupancy of NVP/C-MSs sample indicates its improved packing density among the samples. Further, taking the as-prepared NVP/C-5-48 and NVP/C-25-48 products

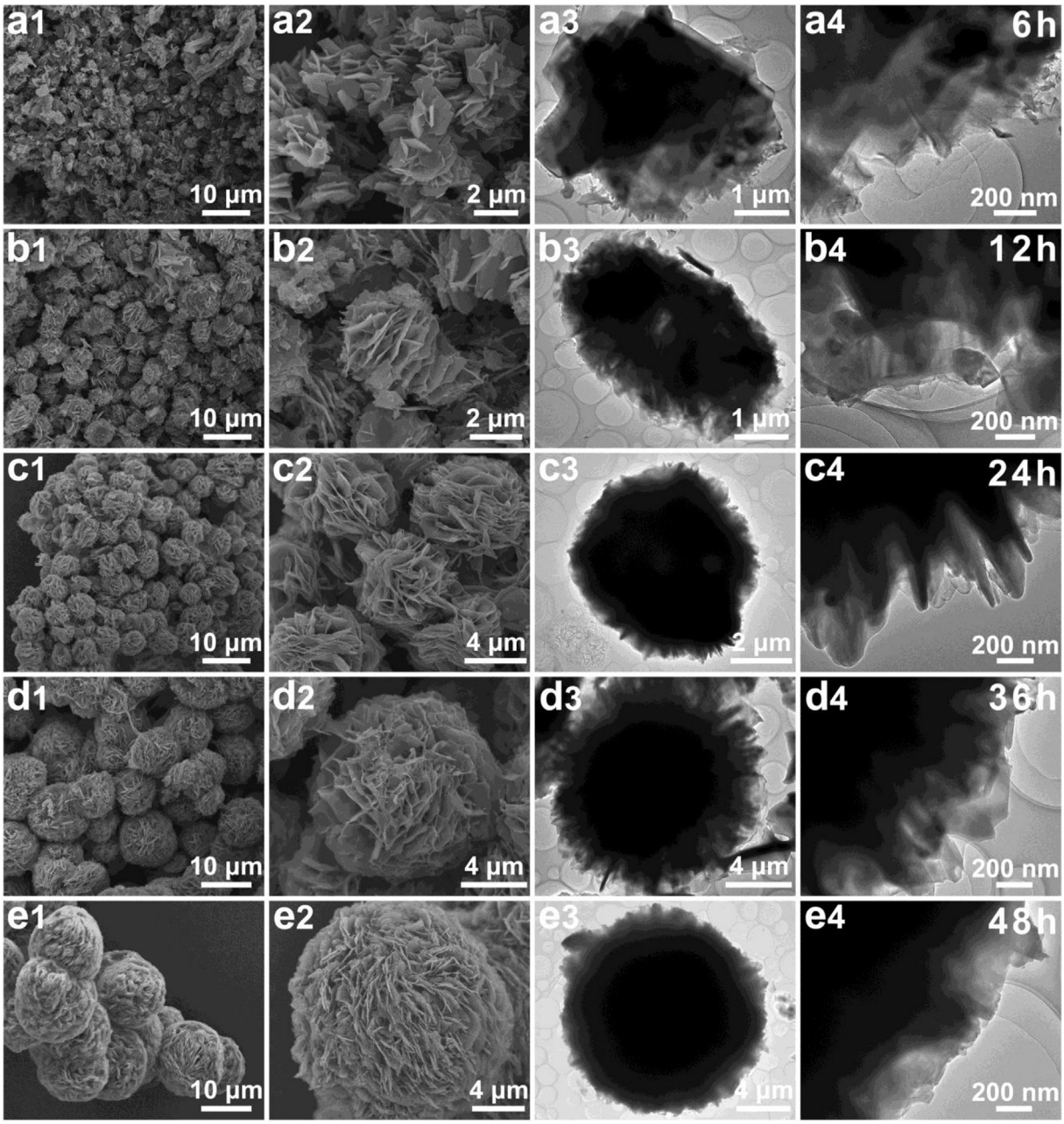

Fig. 3. The different hydrothermal reaction time affected the morphological evolution process of NVP/C illustrated by FESEM images and TEM images: (a1-a4) NVP/C-15-6, (b1-b4) NVP/C-15-12, (c1-c4) NVP/C-15-24, (d1-d4) NVP/C-15-36, (e1-e4) NVP/C-MSs.

as representatives, the detailed chemical and physical characterizations of them were carried out. The Raman spectra (Figs. S12a and S13a, Supporting Information) of NVP/C-5-48 and NVP/C-25-48 display two characteristic bands of carbonaceous materials located at 1326 cm^{-1} and 1588 cm^{-1}. Also, according to the TGA results (Figs. S12b and S13b, Supporting Information), the amounts of carbon in NVP/C-5-48 and NVP/C-25-48 products are about 9.8 wt% and 9.96 wt%, respectively. The XPS spectra of the NVP/C-5-48 and NVP/C-25-48 products clearly indicate the presence of carbon and nitrogen (Figs. S12e, S12f, S13e, and S13f, Supporting Information). Based on the elemental analysis shown in Table S3 (Supporting Information), NVP/C-5-48 and NVP/C-25-48 display a nitrogen content of 2.12 wt% and 1.99 wt%, respectively, indicating the successful doping of nitrogen into the coated carbon skeleton. The elemental mapping images of NVP/C-25-48 further confirm the existence of nitrogen (Fig. S14, Supporting Information). NVP/C-MSs has a hierarchical porous structure, relatively high BET surface area combined with suitable N-doped carbon coating, which may contribute to better electrochemical performance.

The nanoflake-constructed porous NVP/C microspheres electrodes with continuous electron and Na ion transfer channels exhibit superior high-rate capability and cycling stability in SIBs (Fig. S1a, Supporting Information). The NVP/C products were first assembled into half-cells to evaluate their electrochemical performances as cathode materials for SIBs and the results are shown in Fig. 6. The rate capability of the five NVP/C products is compared firstly. As shown in Fig. 6a, the average reversible capacity of NVP/C-MSs electrode at a current rate of 0.5 C is 116.3 mA h g^{-1}, much higher than those of NVP/C-5-48 (112.3 mA h g^{-1}), NVP/C-10-48 (114.8 mA h g^{-1}), NVP/C-20-48 (103 mA h g^{-1}), and NVP/C-25-48 (101.3 mA h g^{-1}). Here 1C refers to 117.6 mA g^{-1}. Along with the increase of the rate from 1 C to 10 C, the specific capacity of the NVP/C-MSs electrode decreases from 114.7 to 109.8 mA h g^{-1}. The decline of capacity with increasing charge/

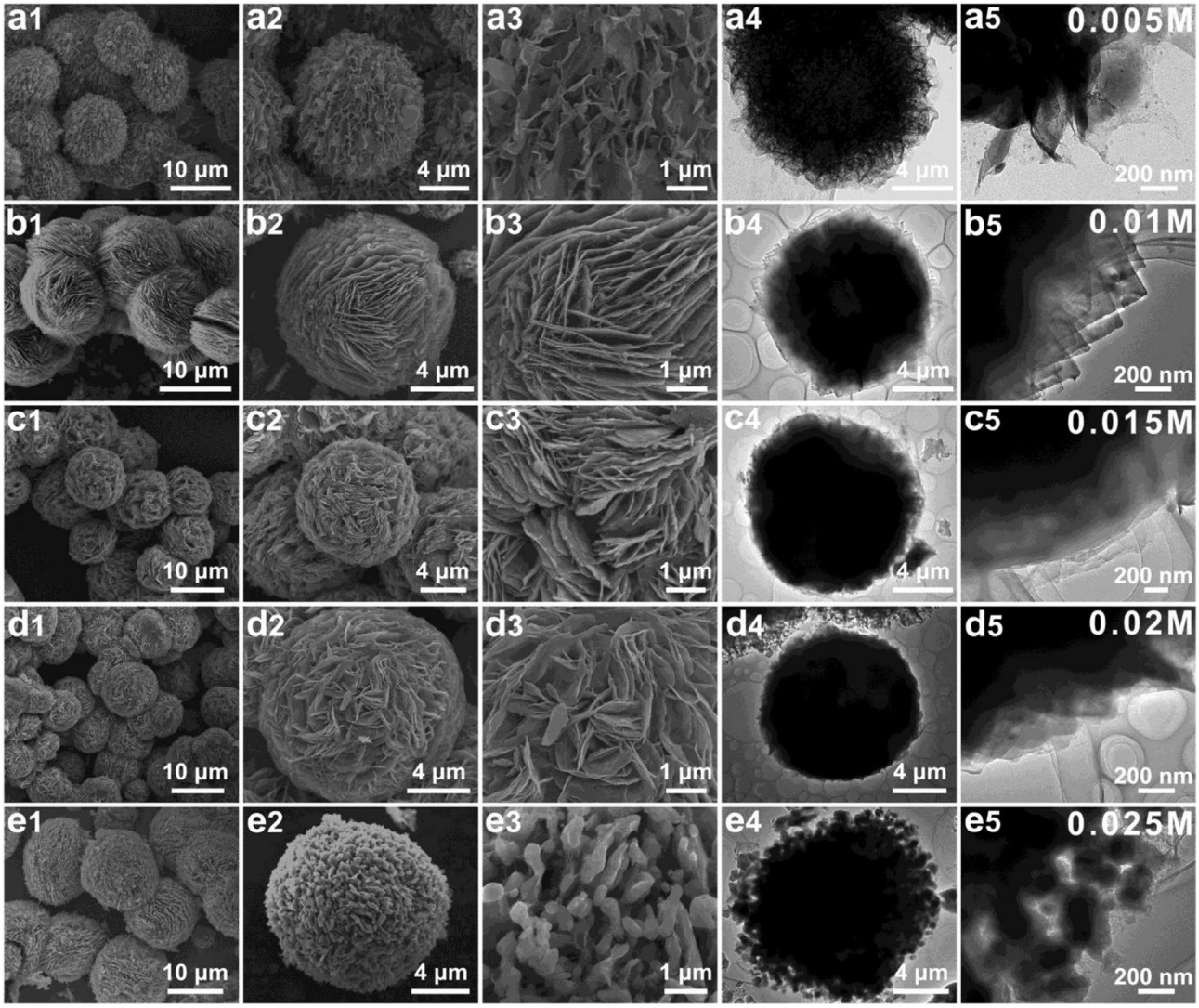

Fig. 4. The different concentrations of precursors affected the morphology and microstructure of NVP/C illustrated by FESEM images and TEM images: (a1-a5) NVP/C-5-48, (b1-b5) NVP/C-10-48, (c1-c5) NVP/C-MSs, (d1-d5) NVP/C-20-48, (e1-e5) NVP/C-25-48.

discharge rate is routinely observable for mass transport limiting process. Impressively, superior high-rate capability is achieved at even ultrahigh rates, delivering 105.6 mA h g^{-1} at 50 C and 99.3 mA h g^{-1} at 100 C, respectively. After the high-rate charge/discharge at 100 C, the average capacity of NVP/C-MSs electrode can be recovered fully when scanned again at 0.5 C, highlighting the excellent Na^+ storage reversibility. On the contrary, NVP/C-5-48, NVP/C-10-48, NVP/C-20-48, and NVP/C-25-48 not only deliver degradative discharge capacities of 68.3, 85.3, 36.7 and 16.8 mA h g^{-1} at the high rate of 100 C, respectively, but also do not recover their initial capacities even when the current rate is reverted to 0.5 C. Fig. 6b shows representative charge/discharge voltage profiles of NVP/C-MSs at various rates. Even at the rates larger than 10 C, the plateaus are still clearly visible. Moreover, compared with the other four samples, the lowest plateau voltage difference at different rates for the NVP/C-MSs electrode suggests the least polarization of it (Fig. 6b; Fig. S15 and Table S5, Supporting Information). The superior rate capability of NVP/C-MSs can be ascribed to the advantages of ionic properties and favorable structure. The nanoflake-constructed hierarchical architecture with large surface area and numerous mesopores can possess large electrode-electrolyte contact area and short ion diffusion distance, thereby facilitating the ionic transport (discussed in detail below). The electronic conduction network established by N-doped carbon layer ensures the fast electron transport (discussed in detail below).

In order to evaluate the potential for practical applications of the NVP/C-MSs cathode, we calculated its power and energy densities based on the capacities at various rates, working potential, and the mass of cathode material. Fig. 6c shows Ragone plots of our NVP/C-MSs cathode, as well as some advanced LIBs and SIBs cathode (normalized to the weight of cathode materials). The NVP/C-MSs cathode can achieve a high energy density of 382.9 W h kg^{-1} at a low power density of 392.5 W kg^{-1}, and even be able to maintain 82.5% gravimetric energy (316 W h kg^{-1}) when the power is increased two orders of magnitude (i.e., 36.7 kW kg^{-1}, charge/discharge time of 36 s), indicating that high power and energy density can be achieved simultaneously. Such performance is comparable to the current state-of-the-art cathode materials such as $LiFePO_4$ microsphere [58], $LiNi_{0.5}Mn_{0.5}O_2$ [59], $Na_3Ni_2SbO_6$ [60], $Na_3V_2(PO_4)_2F_3$/C [61], $Na_3V_2(PO_4)_3$ microsphere [62], $Na_3V_2(PO_4)_3$/C/rGO [31], $Na_3V_2(PO_4)_3$/C-N [63], and $Na_3V_2(PO_4)_3$/rGO [64].

Fig. 6d exhibits the initial five successive CV curves of NVP/C-MSs electrode at a scan rate of 0.1 mV s^{-1}. A pair of well-defined oxidation/reduction peaks at 3.48/3.33 V for NVP/C-MSs can be seen in the first and subsequence cycles, which are assigned to the Na^+ extraction/insertion out/in of the $Na_3V_2(PO_4)_3$ host structure ($Na_3V_2(PO_4)_3$ ↔ $NaV_2(PO_4)_3$) [39,56]. Besides, the redox peak profile of NVP/C-MSs is

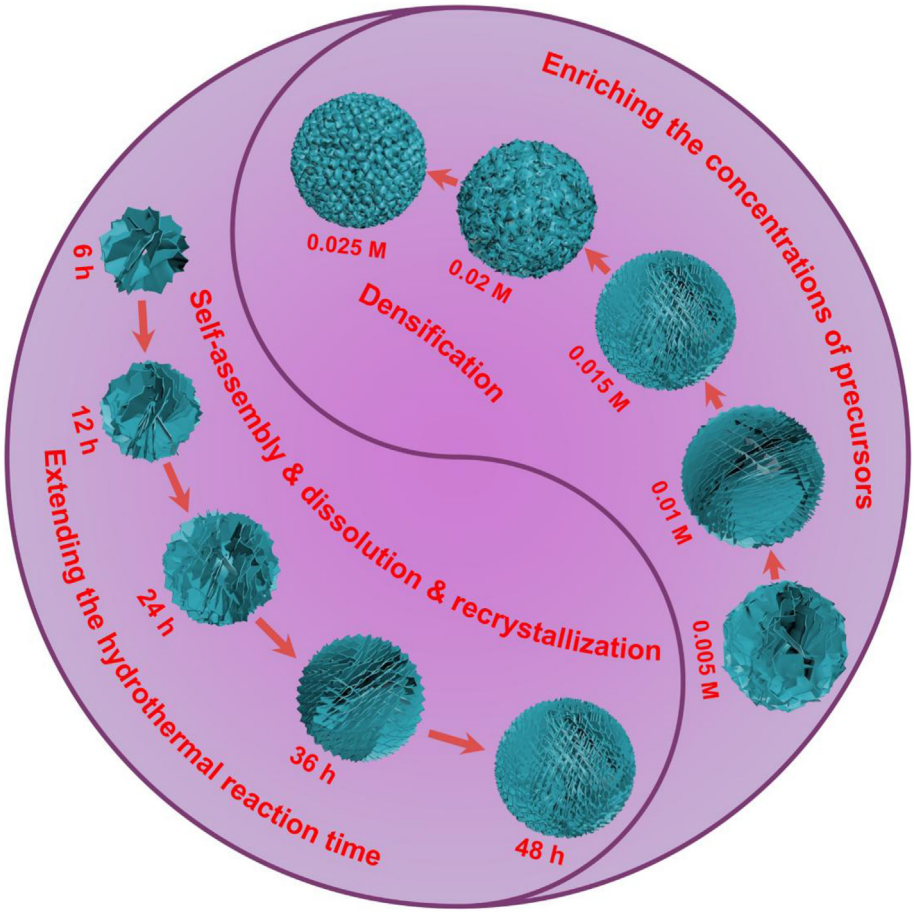

Fig. 5. Schematic illustration of the formation process for hierarchical microspheres with various sizes and building blocks.

sharp and symmetric, indicating good reversibility and small polarization of the electrode [65]. The galvanostatic charge/discharge voltage profiles of the NVP/C-MSs electrodes at current rates of 1 C and 5 C in the potential window of 2.5–4.0 V (vs. Na^+/Na) are displayed in Fig. 6e. The potentials of the charge/discharge plateaus are in good agreement with the CV results. The NVP/C-MSs electrode exhibits the initial charge and discharge capacities of 117 and 115.6 mA h g^{-1} at 1 C, respectively, corresponding to a high Coulombic efficiency of 98.8%. When the rate is increased to 5C, it can still retain initial charge and discharge capacities of 113 and 111.3 mA h g^{-1} with a Coulombic efficiency of 98.5%. This initial irreversibility may be attributed to the electrolyte decomposition and other undesirable side reactions [15,66]. Cycling stability is critical for the electrodes in practical applications. Our NVP/C-MSs electrode exhibits exceptionally high stability. After 1000 cycles of charge/discharge at 1C, the initial capacity of 115.6 mA h g^{-1} is reduced to 109.5 mA h g^{-1} with a capacity retention of 94.7% (Fig. 6f). At a high rate of 5 C, 102.3 mA h g^{-1} is maintained with a 91.9% retention after 1000 cycles (Fig. 6f). To demonstrate the potential of high-power application of NVP/C-MSs electrode, we conducted the long-term ultrafast charge/discharge ability (Fig. 6g). The NVP/C-MSs deliver an initial specific discharge capacity of 109.5 mA h g^{-1} at the rate of 20 C and retain a capacity of 86.6 mA h g^{-1} after 10000 cycles, corresponding to the capacity retention of 79.1% and average capacity fading rate of 0.002% per cycle. Additionally, the average coulombic efficiency is close to 100%, indicating the superior phase reversibility of the NVP/C-MSs material during repeated extraction/insertion of Na^+ even at long-term high-rate cycling. Fig. S16 (Supporting Information) shows the cycling performance and rate capability of NVP/C-MSs cathode with different areal mass loading. Even at a high active material mass loading of 3.7 mg cm^{-2}, only a slight capacity loss is observed, further indicating the high availability of the active material. Such excellent specific capacity, rate capability, and cyclic stability are superior to the state-of-the-art reported NVP cathodes (Table S6, Supporting Information), suggesting the synergistic effect of improved electron/ion transfer kinetics introduced by homogeneous N-doped carbon coating and large interstitial space, and attractive structure integrity as well as large surface area resulted from hierarchical microsphere morphology.

In order to gain further insight into the enhanced electrochemical performance of the nanoflake-constructed porous NVP/C microspheres electrodes, CV, Galvanostatic intermittent titration technique (GITT), EIS, as well as *ex situ* XRD, SEM, and TEM characterizations were carried out. Fig. S17 (Supporting Information) displays the typical CV curves at the scan rates of 0.1–1.0 mV s^{-1} along with the relationship between the peak current (*Ip*) and the square roots of scan rates ($v^{1/2}$). As the scan rate increased, the intensities of redox peaks also increase, while the anodic and cathodic peaks move toward the higher and lower potentials, respectively. The apparent diffusion coefficients of Na^+ in solid state composite are calculated based on the classical Randles-Sevchik equation (Note S1, Supporting Information) and are listed in Table S7 (Supporting Information). The diffusion coefficients of NVP/C-MSs electrode can reach $\approx 10^{-9}$ cm^2 s^{-1} for both anodic and cathodic processes, which are almost an order of magnitude higher than NVP/C-5-48 and NVP/C-10-48 electrodes, as well as two orders of magnitude higher than those of NVP/C-20-48 and NVP/C-25-48 electrodes. As shown in Fig. S18 (Supporting Information), the Na^+ diffusion coefficients in NVP/C-MSs are minor fluctuant and higher than those in other NVP/C electrodes as a whole, which is similar to the CV results. The excellent Na^+ diffusion behavior of NVP/C-MSs would improve the extraction/insertion reaction kinetics [31,67,68]. The EIS spectra after

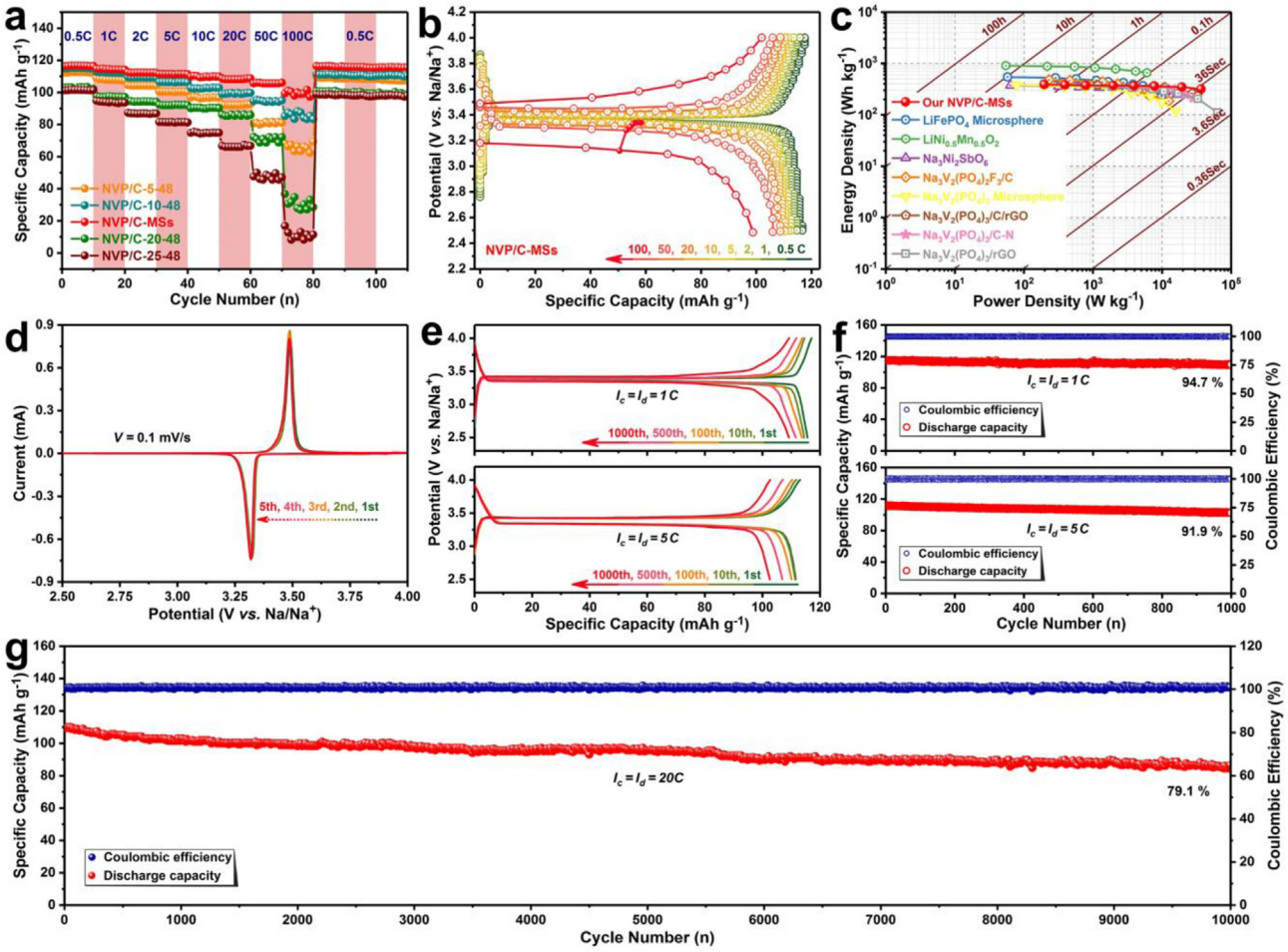

Fig. 6. The electrochemical characterization of the NVP/C microspheres as a half-cell cathode in the potential ranging from 2.5 to 4 V versus Na/Na^+. (a) Rate performances of these five electrodes at various current densities from 0.5 to 100 C (1 C = 117.6 mA g^{-1}). (b) Galvanostatic charge/discharge profiles of NVP/C-MSs at various current densities. (c) Ragone plots of our NVP/C-MSs cathode, compared with some advanced LIBs and SIBs cathode materials ($LiFePO_4$ microsphere‖Li [58], $LiNi_{0.5}Mn_{0.5}O_2$‖Li [59], $Na_3Ni_2SbO_6$‖Na [60], $Na_3V_2(PO_4)_2F_3/C$‖Na [61], $Na_3V_2(PO_4)_3$ microsphere‖Na [62], $Na_3V_2(PO_4)_3$/C/rGO‖Na [31], $Na_3V_2(PO_4)_3$/C-N‖Na [63], and $Na_3V_2(PO_4)_3$/rGO‖ Na [64]). (d) CV curves of the initial five cycles of the NVP/C-MSs electrode at a scan rate of 0.1 mV s^{-1}. (e) Galvanostatic charge/discharge profiles from selected cycles of the NVP/C-MSs electrodes at 1C and 5C, respectively. (f) Cycling performance and Coulombic efficiency of the NVP/C-MSs electrodes measured at 1C and 5 C for 1000 cycles. (g) Long-term cycling performance and Coulombic efficiency of the NVP/C-MSs electrode at 20 C for 10,000 cycles.

the first cycle show that charge-transfer resistance (R_{ct}) of NVP/C-MSs is only 223.6 Ω, lower than those of the NVP/C-5-48 (244.5 Ω), NVP/C-10-48 (270.4 Ω), NVP/C-20-48 (301.3 Ω), and NVP/C-25-48 (331.4 Ω) electrodes (Fig. S21 and Table S8, Supporting Information). The EIS of NVP/C-MSs is monitored during first to 1000th cycles, as shown in Fig. S22 (Supporting Information). The fitted sodium R_{ct} and the calculated Na^+ diffusion coefficients corresponding to the Nyquist plots after different cycles are shown in Table S9 (Supporting Information). Even after 1000 cycles, only a small impedance increase is detected. This indicates that the existence of highly conductive N-doped carbon network indeed improves the charge transfer kinetics. Moreover, even after 1000 cycles, the NVP/C-MSs electrode still exhibits rapid ion diffusion rate (1.16×10^{-10} cm^2 s^{-1}). The *ex situ* XRD patterns of NVP/C electrodes after rate-capability tests (Fig. S23, Supporting Information) show that, all the diffraction peaks can be well indexed to the rhombohedral NVP phase without any impurities, implying the excellent maintenance of NASICON crystal structure and no side reactions during the rapid charge/discharge process. The morphological and structural changes of the NVP/C electrodes after 1000 cycles at 5 C are further studied by *ex situ* SEM and TEM (Fig. S24, Supporting Information). The morphology of NVP/C-MSs is still maintained without any obvious pulverization or size variation even after 1000 charge/discharge cycles (Figures S24b1-b3, Supporting Information). From the HRTEM image (Figure S24b4, Supporting Information), the crystal structure of NVP and the N-doped carbon protection still maintain integral. Although the single-crystal structure of the NVP/C-5-48 and NVP/C-25-48 electrodes can be generally maintained (Figures S24a4 and S24c4, Supporting Information), they suffered serious aggregation or pulverization (Figures S24a1-a3 and S24c1-c3, Supporting Information), leading to the unstable interface, electrical contact loss between active material and current collector, and the capacity decay. Such robust 3D microsphere architecture of NVP/C-MSs composite, as mentioned before, can significantly promote ultrafast electronic transport and ion diffusion, as well as accommodate the volume variations during cycling.

Encouraged by the excellent performance of the NVP/C-MSs electrode in the half-cell test, we further fabricated the sodium-ion full-cell using NVP/C-MSs as the cathode and self-made SnS/C fibers as the anode [69]. Before full cell assembly, the crystal structure and microstructure (Fig. S25, Supporting Information), and electrochemical performance (Fig. S26, Supporting Information) of the SnS/C fibers are also presented. The orange areas of Fig. 7a, c shows the CV and the corresponding charge/discharge curves of the aforementioned NVP/C-MSs/Na configuration. The green area in Fig. 7a shows the CV curve of

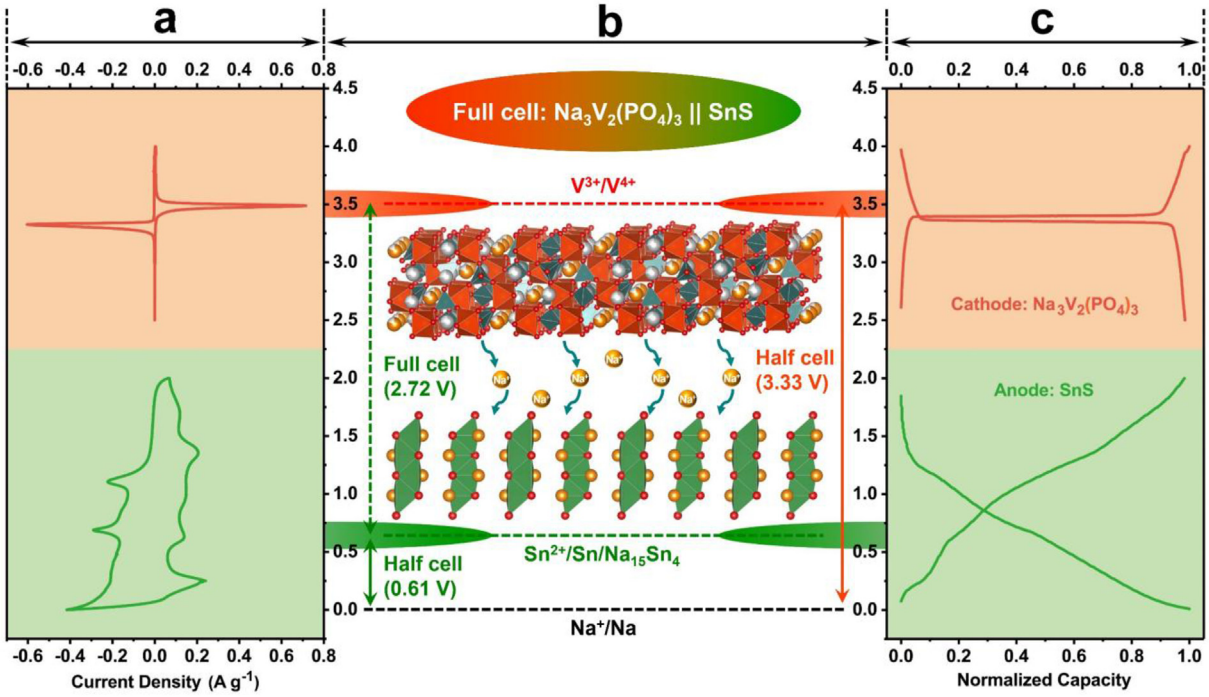

Fig. 7. The electrochemical performance of NVP/C-MSs and SnS/C electrodes in the half-cell format versus Na^+/Na. The (a) CV and (c) galvanostatic charge/discharge curves of NVP/C-MSs in the potential range of 2.5–4 V (orange) and SnS/C in the voltage range of 0.001–2 V (green) versus Na^+/Na, respectively. (b) Schematic of potential of the V^{4+}/V^{3+} redox couple versus Na^+/Na in NVP and $Sn^{2+}/Sn/Na_{15}Sn_4$ conversion & alloying couples vs. Na^+/Na in layered SnS materials. Insets in (b) display the crystal structures of NVP and SnS, the average potentials of the NVP and SnS/Na half cells as cathode and anode, respectively, and further predict the average working voltage of ≈2.72 V for the NVP ‖ SnS sodium-ion full-cells.

the SnS/C in the voltage range between 0.001 V and 2.0 V with multi-step alloying/dealloying redox peaks and conversion reaction peaks [70,71]. Accordingly, the discharge/charge curve is displayed in the green area of Fig. 7c, and the apparent steps are also validated by the CV curve. Fig. 7b shows the schematic of electric potential for the V^{4+}/V^{3+} redox couple *vs.* Na^+/Na in NVP and $Sn^{2+}/Sn/Na_{15}Sn_4$ conversion & alloying couples *vs.* Na^+/Na in layered SnS materials. The average potential of this asymmetric cell based on the NVP cathode and SnS anode is predicted on the basis of their voltage difference, shown in the inset of Fig. 7b.

Fig. 8a shows the typical charge/discharge profiles of the sodium-ion full-cell at a current density of 200 mA g^{-1} based on the weight of NVP/C-MSs. The full-cell displays fastigiate charge/discharge voltage plateaus with initial charge/discharge capacities of 104 and 102 mA h g^{-1}, respectively. The inset of Fig. 8a shows a commercial blue light-emitting diode (LED) on Central South University (CSU) logo powered by the assembled full cells. As shown in Fig. 8b, the sodium-ion full-cell delivers an initial specific discharge capacity of 102 mA h g^{-1} at 200 mA g^{-1} based on the weight of NVP/C-MSs cathode. After 500 cycles, it still can retain 76.1 mA h g^{-1}, 74.6% of its original capacity, indicating the outstanding cycling stability of the NVP/C-MSs ‖ SnS/C sodium-ion full-cell. The rate capability test shown in Fig. 8c demonstrates that the full cell can be effectively cycled at various current densities from 100 mA g^{-1} to 2000 mA g^{-1}. The capacity varies from 107.5 mA h g^{-1} at 100 mA g^{-1} to 95.3 mA h g^{-1} at 500 mA g^{-1}. Even with a discharge current density of 2000 mA g^{-1}, the discharge capacity remains at 62 mA h g^{-1}, approximately 58% of the reversible capacity at a current density of 100 mA g^{-1}. Fig. 8d and e and Table S10 (Supporting Information) summarize many recently reported sodium-ion full-cell configurations, in which main electrochemical parameters, such as cell voltage, capacity, energy density and power density, are included. Our NVP/C-MSs ‖ SnS/C sodium-ion full-cell exhibits a maximum energy density of about 223 W h kg^{-1} (with power density 249 W kg^{-1}) and a maximum power density of 3488 W kg^{-1} (with energy density 90 W h kg^{-1}). Overall, the above-emphasized features enable the device's superior electrochemical performance, which is at least comparable to and probably slightly better than the state-of-the-art reported sodium-ion full-cell configurations, such as $VOPO_4$‖$Na_2Ti_3O_7$ [72], $Na_{1.92}Fe_2(CN)_6$‖hard carbon [73], NVOPF‖VO_2 [74], symmetric $Na_{0.8}Ni_{0.4}Ti_{0.6}O_2$ [75], symmetric $Na_{0.6}[Cr_{0.6}Ti_{0.4}]O_2$ [14], symmetric NVP@C [76], NVP/C‖NTP@rGO [28], NVP-F‖NTP [34], NVP/C‖$Na_{0.66}[Li_{0.22}Ti_{0.78}]O_2$ [15], and symmetric $Na_{0.66}Ni_{0.17}Co_{0.17}Ti_{0.66}O_2$ [77].

4. Conclusions

In summary, we have developed a convenient strategy that combines hydrothermally assisted self-assembly along with subsequent *in situ* crystallization and N-doped carbon coating to synthesize novel hierarchical porous microspheres (NVP/C-MSs) by using sodium oleate as both sodium source and structure-directing agent. The effects of hydrothermal reaction time and concentrations of precursor solution on the micro/nano structure of the NVP products are studied in detail and the morphological evolution mechanism is proposed. Such novel micro/nano architecture can not only provide bicontinuous electron/ion pathways and large electrode-electrolyte contact area, but also provides an increased tap density as compared to nanomaterials. Meanwhile, the robust structure stability relieves the volume deformation during repeated Na^+ extraction/insertion processes. As a result, the optimum NVP/C-MSs exhibits excellent electrochemical performance for both sodium-ion half-cell and full-cell. For instance, a high capacity of 116.3 mA h g^{-1} at a rate of 0.5 C, a considerable capacity of 99.3 mA h g^{-1} at a high rate of 100 C, and excellent cyclic stability up to 10,000 cycles at 20 C can be achieved for half-cell. More importantly, the fabricated NVP-/CMSs ‖ SnS/C full-cell demonstrates a practical estimated energy density of 223 W h kg^{-1} and long-term cyclability. Our encouraging results may boost further development of SIBs technology by smart engineering of the electrode materials.

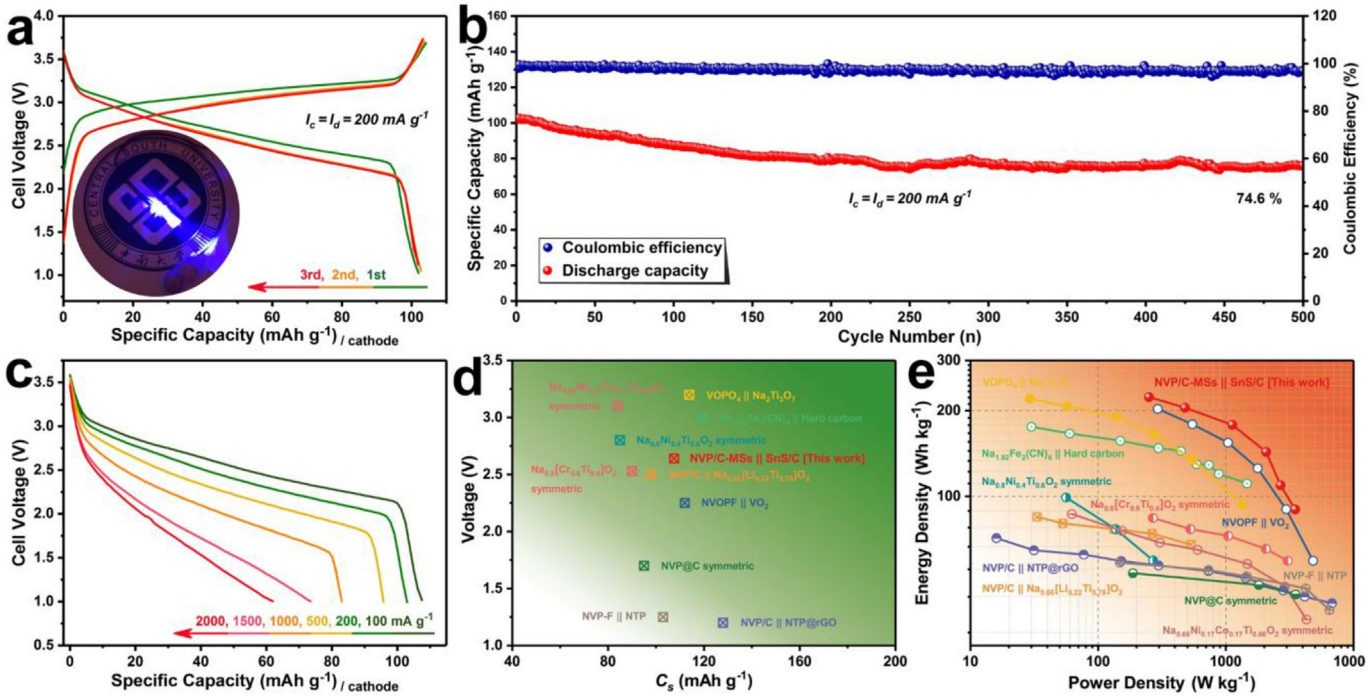

Fig. 8. Electrochemical performance of the assembled NVP/C-MSs ‖ SnS/C sodium-ion full-cells. (a) The typical galvanostatic charge/discharge profiles in the potential range of 1–3.7 V at a current density of 200 mA g^{-1}. The inset shows a commercial blue LED powered by the assembled full cells. (b) The capacity retention with Coulombic efficiency at the current density of 200 mA g^{-1} showing the outstanding cycling performance (74.6% capacity retention after 500 cycles). (c) The capacity at various current densities from 100 mA g^{-1} to 2000 mA g^{-1}. (d) The comparison of voltage and capacity for the NVP/C-MSs ‖ SnS/C sodium-ion full-cell with other recently reported literature. (e) Ragone plots comparing the NVP/C-MSs ‖ SnS/C sodium-ion full-cell with other state-of-the-art reported sodium-ion full-cell configurations. The energy and power densities are based on the total mass of cathode and anode active materials ($VOPO_4$‖$Na_2Ti_3O_7$ [72], $Na_{1.92}Fe_2(CN)_6$‖Hard carbon [73], NVOPF‖VO_2 [74], Symmetric $Na_{0.8}Ni_{0.4}Ti_{0.6}O_2$ [75], Symmetric $Na_{0.6}[Cr_{0.6}Ti_{0.4}]O_2$ [14], Symmetric NVP@C [76], NVP/C‖NTP@rGO [28], NVP-F‖NTP [34], NVP/C‖$Na_{0.66}[Li_{0.22}Ti_{0.78}]O_2$ [15], Symmetric $Na_{0.66}Ni_{0.17}Co_{0.17}Ti_{0.66}O_2$ [77]).

Acknowledgements

This work was supported by the National Natural Science Foundation of China (Grant Nos. 51872334, 51874362, and 51572299), the Program for New Century Excellent Talents in University (Grant No. NCET-13-0594), the Innovation-Driven Project of Central South University (Grant Nos. 2017CX001, and 2018CX004), and the Natural Science Foundation of Hunan Province, China (Grant No. 2018JJ1036).

Appendix A. Supplementary data

Supplementary data to this article can be found online at https://doi.org/10.1016/j.nanoen.2019.03.066.

References

[1] J. Meng, H. Guo, C. Niu, Y. Zhao, L. Xu, Q. Li, L. Mai, Joule 1 (2017) 522–547.
[2] J. Goodenough, Energy Storage Mater. 1 (2015) 158–161.
[3] E. Evarts, Nature 526 (2015) S93–S95.
[4] B. Dunn, H. Kamath, J. Tarascon, Science 334 (2011) 928–935.
[5] X. Han, X. Gui, T. Yi, Y. Li, C. Yue, Curr. Opin. Solid State Mater. Sci. 22 (2018) 109–126.
[6] T. Yi, Y. Zhu, W. Tao, S. Luo, Y. Xie, X. Li, J. Power Sources 399 (2018) 26–41.
[7] Y. Fang, L. Xiao, Z. Chen, X. Ai, Y. Cao, H. Yang, Electrochem. Energy Rev. 1 (2018) 294–323.
[8] J. Hwang, S. Myung, Y. Sun, Chem. Soc. Rev. 46 (2017) 3529–3614.
[9] H. Hou, C. Banks, M. Jing, Y. Zhang, X. Ji, Adv. Mater. 27 (2015) 7861–7866.
[10] J. Ma, F. Li, Z. Wei, Y. Feng, A. Manthiram, L. Mai, J. Mater. Chem. A (2019), https://doi.org/10.1039/C8TA11999F.
[11] Y. Sun, L. Zhao, H. Pan, X. Lu, L. Gu, Y. Hu, H. Li, M. Armand, Y. Ikuhara, L. Chen, X. Huang, Nat. Commun. 4 (2013) 1870.
[12] N. Yabuuchi, M. Kajiyama, J. Iwatate, H. Nishikawa, S. Hitomi, R. Okuyama, R. Usui, Y. Yamada, S. Komaba, Nat. Mater. 11 (2012) 512–517.
[13] Y. You, A. Manthiram, Adv. Energy Mater. 8 (2018) 1701785.
[14] Y. Wang, R. Xiao, Y. Hu, M. Avdeev, L. Chen, Nat. Commun. 6 (2015) 6954.
[15] Y. Wang, X. Yu, S. Xu, J. Bai, R. Xiao, Y. Hu, H. Li, X. Yang, L. Chen, X. Huang, Nat. Commun. 4 (2013) 2365.
[16] Z. Jian, Y. Hu, X. Ji, W. Chen, Adv. Mater. 29 (2017) 1601925.
[17] S. Chen, C. Wu, L. Shen, C. Zhu, Y. Huang, K. Xi, J. Maier, Y. Yu, Adv. Mater. 29 (2017) 1700431.
[18] Y. Fang, Q. Liu, L. Xiao, Y. Rong, Y. Liu, Z. Chen, X. Ai, Y. Cao, H. Yang, J. Xie, C. Sun, X. Zhang, B. Aoun, X. Xing, X. Xiao, Y. Ren, Chem 4 (2018) 1167–1180.
[19] H. Luong, T. Pham, Y. Morikawa, Y. Shibutani, V. Dinh, Phys. Chem. Chem. Phys. 20 (2018) 23625–23634.
[20] L. Wang, Y. Lu, J. Liu, M. Xu, J. Cheng, D. Zhang, J. Goodenough, Angew. Chem. Int. Ed. 52 (2013) 1964–1967.
[21] C. Wessells, R. Huggins, Y. Cui, Nat. Commun. 2 (2011) 550.
[22] Y. Xu, M. Zhou, Y. Lei, Mater. Today 21 (2018) 60–78.
[23] M. Lee, J. Hong, J. Lopez, Y. Sun, D. Feng, K. Lim, W. Chueh, M. Toney, Y. Cui, Z. Bao, Nat. Energy 2 (2017) 861–868.
[24] S. Wang, L. Wang, Z. Zhu, Z. Hu, Q. Zhao, J. Chen, Angew. Chem. Int. Ed. 53 (2014) 5892–5896.
[25] Y. Cai, X. Cao, Z. Luo, G. Fang, F. Liu, J. Zhou, A. Pan, S. Liang, Adv. Sci. 5 (2018) 1800680.
[26] Z. Jian, C. Yuan, W. Han, X. Lu, L. Gu, X. Xi, Y. Hu, H. Li, W. Chen, D. Chen, Y. Ikuhara, L. Chen, Adv. Funct. Mater. 24 (2014) 4265–4272.
[27] C. Liu, R. Masse, X. Nan, G. Cao, Energy Storage Mater. 4 (2016) 15–58.
[28] Y. Fang, L. Xiao, J. Qian, Y. Cao, X. Ai, Y. Huang, H. Yang, Adv. Energy Mater. 6 (2016) 1502197.
[29] X. Wang, C. Niu, J. Meng, P. Hu, X. Xu, X. Wei, L. Zhou, K. Zhao, W. Luo, M. Yan, L. Mai, Adv. Energy Mater. 5 (2015) 1500716.
[30] Y. Fang, L. Xiao, X. Ai, Y. Cao, H. Yang, Adv. Mater. 27 (2015) 5895–5900.
[31] X. Rui, W. Sun, C. Wu, Y. Yu, Q. Yan, Adv. Mater. 27 (2015) 6670–6676.
[32] Y. Jiang, X. Zhou, D. Li, X. Cheng, F. Liu, Y. Yu, Adv. Energy Mater. 8 (2018) 1800068.
[33] W. Shen, C. Wang, Q.J. Xu, H.M. Liu, Y.G. Wang, Adv. Energy Mater. 5 (2015) 1400982.
[34] W. Ren, Z. Zheng, C. Xu, C. Niu, Q. Wei, Q. An, K. Zhao, M. Yan, M. Qin, L. Mai, Nano Energy 25 (2016) 145–153.
[35] Y. Zhou, X. Rui, W. Sun, Z. Xu, Y. Zhou, W. Ng, Q. Yan, E. Fong, ACS Nano 9 (2015) 4628–4635.
[36] L. Zhou, K. Zhang, Z. Hu, Z. Tao, L. Mai, Y. Kang, S. Chou, J. Chen, Adv. Energy Mater. 8 (2018) 1701415.
[37] M. Zheng, H. Tang, L. Li, Q. Hu, L. Zhang, H. Xue, H. Pang, Adv. Sci. 5 (2018) 1700592.
[38] Y. Zhang, A. Pan, Y. Wang, X. Cao, Z. Zhou, T. Zhu, S. Liang, G. Cao, Energy Storage

Mater. 8 (2017) 28–34.
[39] X. Cao, A. Pan, S. Liu, J. Zhou, S. Li, G. Cao, J. Liu, S. Liang, Adv. Energy Mater. 7 (2017) 1700797.
[40] R. von Hagen, A. Lepcha, X. Song, W. Tyrra, S. Mathur, Nano Energy 2 (2013) 304–313.
[41] M. Yu, Y. Zeng, Y. Han, X. Cheng, W. Zhao, C. Liang, Y. Tong, H. Tang, X. Lu, Adv. Energy Mater. 25 (2015) 3534–3540.
[42] M. Reddy, G. Rao, B. Chowdari, J. Power Sources 195 (2010) 5768–5774.
[43] D. Marton, K. Boyd, A. Al-Bayati, S. Todorov, J. Rabalais, Phys. Rev. Lett. 73 (1994) 118–121.
[44] C. Zhang, L. Fu, N. Liu, M. Liu, Y. Wang, Z. Liu, Adv. Mater. 23 (2011) 1020–1024.
[45] G. Fang, Z. Wu, J. Zhou, C. Zhu, X. Cao, T. Lin, Y. Chen, C. Wang, A. Pan, S. Liang, Adv. Energy Mater. 8 (2018) 1703155.
[46] A. Pan, H. Wu, L. Zhang, X. Lou, Energy Environ. Sci. 6 (2013) 1476–1479.
[47] J. Ye, W. Liu, J. Cai, S. Chen, X. Zhao, H. Zhou, L. Qi, J. Am. Chem. Soc. 133 (2011) 933–940.
[48] Y. Xiao, S. Liu, F. Li, A. Zhang, J. Zhao, S. Fang, D. Jia, Adv. Funct. Mater. 22 (2012) 4052–4059.
[49] B. Yan, X. Li, Z. Bai, Y. Zhao, L. Dong, X. Song, D. Li, C. Langford, X. Sun, Nano Energy 24 (2016) 32–44.
[50] C. Fontenot, J. Wiench, M. Pruski, G. Schrader, J. Phys. Chem. B 104 (2000) 11622–11631.
[51] W. Li, Q. Yue, Y. Deng, D. Zhao, Adv. Mater. 25 (2013) 5129–5152.
[52] W. Li, J. Liu, D. Zhao, Nature Rev. Mater. 1 (2016) 16023.
[53] C. Zhang, Z. Chen, Z. Guo, X. Lou, Energy Environ. Sci. 6 (2013) 974–978.
[54] A. Pan, H. Wu, L. Yu, X. Lou, Angew. Chem. Int. Ed. 125 (2013) 2282–2286.
[55] C. Xu, Y. Xu, C. Tang, Q. Wei, J. Meng, L. Huang, L. Zhou, G. Zhang, L. He, L. Mai, Nano Energy 28 (2016) 224–231.
[56] K. Saravanan, C. Mason, A. Rudola, K. Wong, P. Balaya, Adv. Energy Mater. 3 (2013) 444–450.
[57] G. Zhang, T. Xiong, M. Yan, Y. Xu, W. Ren, X. Xu, Q. Wei, L. Mai, Chem. Mater. 29 (2017) 8057–8064.
[58] S. Oh, S. Myung, S. Oh, K. Oh, K. Amine, B. Scrosati, Y. Sun, Adv. Mater. 22 (2010) 4842–4845.
[59] K. Kang, Y. Meng, J. Breger, C. Grey, G. Ceder, Science 311 (2006) 977–980.
[60] D. Yuan, X. Liang, L. Wu, Y. Cao, X. Ai, J. Feng, H. Yang, Adv. Mater. 26 (2014) 6301–6306.
[61] Q. Liu, D. Wang, X. Yang, N. Chen, C. Wang, X. Bie, Y. Wei, G. Chen, F. Du, J. Mater. Chem. A 3 (2015) 21478–21485.
[62] J. Zhang, Y. Fang, L. Xiao, J. Qian, Y. Cao, X. Ai, H. Yang, ACS Appl. Mater. Interfaces 9 (2017) 7177–7184.
[63] Y. Yao, Y. Jiang, H. Yang, X. Sun, Y. Yu, Nanoscale 9 (2017) 10880–10885.
[64] Y. Xu, Q. Wei, C. Xu, Q. Li, Q. An, P. Zhang, J. Sheng, L. Zhou, L. Mai, Adv. Energy Mater. 6 (2016) 1600389.
[65] Y. Zou, S. Chen, X. Yang, N. Ma, Y. Xia, D. Yang, S. Guo, Adv. Energy Mater. 6 (2016) 1601549.
[66] Y. Fang, L. Xiao, J. Qian, Y. Cao, X. Ai, Y. Huang, H. Yang, Adv. Energy Mater. 6 (2016) 1502197.
[67] S. Liang, X. Cao, Y. Wang, Y. Hu, A. Pan, G. Cao, Nano Energy 22 (2016) 48–58.
[68] X. Cao, A. Pan, Y. Zhang, J. Li, Z. Luo, X. Yang, S. Liang, G. Cao, ACS Appl. Mater. Interfaces 8 (2016) 27632-28640.
[69] Y. Wang, Y. Zhang, J. Shi, X. Kong, X. Cao, S. Liang, G. Cao, A. Pan, Energy Storage Mater. 18 (2019) 366–374.
[70] D. Chao, C. Zhu, P. Yang, X. Xia, J. Liu, J. Wang, X. Fan, S. Savilov, J. Lin, H. Fan, Z. Shen, Nat. Commun. 7 (2016) 12122.
[71] Y. Liu, X. Yu, Y. Fang, X. Zhu, J. Bao, X. Zhou, X. Lou, Joule 2 (2018) 725–735.
[72] H. Li, L. Peng, Y. Zhu, D. Chen, X. Zhang, G. Yu, Energy Environ. Sci. 9 (2016) 3399–3405.
[73] L. Wang, J. Song, R. Qiao, L. Wray, M. Hossain, Y. Chuang, W. Yang, Y. Lu, D. Evans, J. Lee, S. Vail, X. Zhao, M. Nishijima, S. Kakimoto, J. Goodenough, J. Am. Chem. Soc. 137 (2015) 2548–2554.
[74] D. Chao, C. Lai, P. Liang, Q. Wei, Y. Wang, C. Zhu, G. Deng, V. Doan-Nguyen, J. Lin, L. Mai, H. Fan, B. Dunn, Z. Shen, Adv. Energy Mater. 8 (2018) 1800058.
[75] S. Guo, H. Yu, P. Liu, Y. Ren, T. Zhang, M. Chen, M. Ishida, H. Zhou, Energy Environ. Sci. 8 (2015) 1237–1244.
[76] Y. Jiang, Y. Wu, Y. Chen, Z. Qi, J. Shi, L. Gu, Y. Yu, Small 14 (2018) 1703471.
[77] S. Guo, P. Liu, Y. Sun, K. Zhu, J. Yi, M. Chen, M. Ishida, H. Zhou, Angew. Chem. Int. Ed. 54 (2015) 11701–11705.

Xinxin Cao received his Bachelor's degree in Materials science and Engineering from Central South University in 2014. He is now a Ph.D. candidate in School of Materials science and Engineering, Central South University supervised by Prof. Shuquan Liang. His research focuses on the synthesis and application of nanomaterials and composites for clean energy storage, such as high-power/high-energy lithium ion batteries, and sodium ion batteries.

Prof. Anqiang Pan received his B. E. (2005) and D. Phil. (2011) degrees in Materials Physics and Chemistry from Central South University in Prof. Shuquan Liang's group. In 2008, he worked in Prof. Guozhong Cao's group at University of Washington as an exchange student (2008–2009). Then, he got the chance to work in PNNL as a visiting scholar in Dr. Ji-Guang Zhang and Dr. Jun Liu's group (2009–2011). After getting the PhD degree, he joined Prof. Xiongwen (David) Lou's group at Nanyang Technological University as a research fellow (2011–2012). He joined the faculty at Central South University in 2012 and was promoted to a Sheng-Hua Professor in 2013. His current interests are the controllable synthesis of nanostructured materials and their applications in energy storage and conversion devices, such as lithium ion batteries, and supercapacitors.

Bo Yin received his Bachelor's degree in Material Processing and Control Engineering from Xi'an Polytechnic University in 2013. He is now a postgraduate student at the School of Materials Science and Engineering, Central South University. His current research focuses on cobalt-based sulfide and porous carbon material for electrochemical energy storage applications.

Guozhao Fang received his Bachelor's degree in Materials science and Engineering from Central South University in 2014. He is now a Ph.D. candidate in School of Materials science and Engineering, Central South University supervised by Prof. Shuquan Liang. His research focuses on the synthesis of mirco/nano-structured materials and their applications in energy storage, such as lithium (sodium)-ion batteries, supercapacitors and aqueous zinc-ion batteries.

Yaping Wang received her M.S. degree in School of Materials Science and Engineering from Central South University in 2016. Currently, she is a Ph.D. candidate in Central South University. Her current research focuses on high capacity anode materials for lithium/sodium ion batteries.

Xiangzhong Kong is a postgraduate student whose academic director is Prof. Pan. He received his Ph.D. degree in School of Materials Science and Engineering from Central South University in December 2018. He joined in Hunan institute of Science and Technology in 2019. His research interests are Mn-based and Si-based anode materials for lithium-ion batteries.

Prof. Ting Zhu received his B. Eng. in Chemistry of Materials (2007) and M. Eng. in Biomedical Engineering (2010) from Sichuan University, China. In 2014, he obtained his Ph. D. degree from Nanyang Technological University, Singapore. After that, he moved to National University of Singapore to work as a research fellow before he joined Central South University (China) as a professor from 2017. His research interests involve the development of nanostructured functional materials for applications in energy storage and conversion, such as lithium ion batteries, supercapacitors, and photocatalytic/electrocatalytic hydrogen (H_2) production.

Prof. Jiang Zhou received his Bachelor degree (2011), and Ph.D. degree (2015) from Central South University. During 2014–2015, he studied in Prof. Hua Zhang's group at Nanyang Technological University (NTU) as an exchange Ph.D. student. After graduated, he carried out his postdoctoral research in Prof. Ju Li's group at Massachusetts Institute of Technology (MIT) since 2016. He joined Central South University as a Professor in the end of 2017. His research interests are on lithium (sodium)-ion batteries, aqueous zinc-ion batteries, etc.

Prof. Guozhong Cao is the Boeing-Steiner Professor in the Department of Materials Science & Engineering and Clean Energy Institute at the University of Washington (Seattle). He is also an adjunct professor at Beijing Institute of Technology and Lanzhou University. His research mainly focuses on chemical processing of nanomaterials for energy related applications including solar cells, rechargeable batteries and supercapacitors.

Prof. Shuquan Liang received his Ph.D. degree from Central South University (P. R. China) in 2000. He was the Dean of School of Materials Science and Engineering in Central South University from October 2010 to January 2019. He is the winner of Monash University Engineering Sir John Medal. He hosted 5 state research projects including national 973 sub-project and national 863 project. He has published more than 100 papers in frontier journals. Currently, his main research interests include micro/nanostructured functional materials, nanocomposites and their energy storage and conversion devices.